Journal of Wind Engineering & Industrial Aerodynamics 224 (2022) 104943

Contents lists available at ScienceDirect

Journal of Wind Engineering & Industrial Aerodynamics

journal homepage: www.elsevier.com/locate/jweia

Environmental contours for wind-resistant bridge design in complex terrain

Dario Fernandez Castellon [a,*], Aksel Fenerci [b], Ole Øiseth [a]

[a] Department of Structural Engineering, Norwegian University of Science and Technology, Richard Birkelands Vei 1A, Trondheim, Norway
[b] Department of Ocean Operations and Civil Engineering, Norwegian University of Science and Technology, Larsgårdsvegen 2, 6025, Ålesund, Norway

A B S T R A C T

Accurate estimation of the extreme wind fields is crucial for long-span bridge design. The current practice is focused on estimating the extreme mean wind speed, neglecting the inherent uncertainty in the turbulence model parameters. However, full-scale measurements on bridges show that such uncertainties are significant and should be considered in design. Here, the environmental contour method (ECM) is used to obtain long-term extreme wind fields considering uncertainties from the mean wind speed, turbulence intensities and spectral parameters measured at the Sulafjord Bridge site. Design contours of combinations of wind field parameters are obtained for target return periods of 4, 50 and 100 years. The contours are based on a proposed probabilistic modeling strategy that combines hindcast mesoscale simulations and field measurements. The contour estimates are also compared with state-of-the-art design values from the design recommendations. It is concluded that the environmental contours provide a more complete and yet intuitive description of the wind field at the bridge site compared to the current design methodology. The ECM is found suitable for obtaining design wind fields at new long-span bridge sites as it makes use of the limited site data more efficiently and it is still easy-to-use for the practicing engineer.

1. Introduction

General practice in bridge design establishes the structural response based on extreme values of wind speeds for long-term return periods (CEN, 2004). In the current design practice, the corresponding design wind loads are estimated using the mean wind speed as the sole stochastic variable, whereas other turbulence-related parameters are treated deterministically, usually dependent on the mean wind speed. However, monitoring campaigns in complex terrain showed that most of the scatter in measured structural response is strongly related to randomness in turbulence-related parameters (Fenerci et al., 2017). The observations show that the extreme structural response does not necessarily occur at the extreme value of mean wind speed but at relatively lower wind speeds with more severe turbulence parameters, such as turbulence intensity. Site measurements of wind and bridge response expose the necessity of design methodologies that consider the stochastic variability in wind variables, such as turbulence intensities, spectral parameters, spatial correlation of turbulence, and incoming wind direction together with the usual mean wind speed (Wang et al., 2013), (Li et al., 2021).

Relevant studies on wind characterization with probabilistic turbulence modeling are not abundant (Fenerci and Øiseth, 2018), (Solari and Piccardo, 2001). On the other hand, there are many studies in the literature about the assessment of structural wind-induced effects using probabilistic frameworks; however, the randomness is usually limited to the structural or aerodynamic parameters and the mean wind speed (Davenport, 1983; Solari, 1997; Pagnini and Solari, 2002; Pagnini, 2010; Seo and Caracoglia, 2012, 2013; Kareem, 1987; Ciampoli et al., 2011). Uncertainty in turbulence itself has been overlooked except for a few studies (Solari and Piccardo, 2001), (Lystad et al., 2018). In that regard, Lystad et al. used the environmental contour method (ECM) to estimate extreme wind fields for the Hardanger Bridge site (Lystad et al., 2020). The ECM obtains combinations of environmental parameters with a selected return period from their joint distribution (Winterstein et al., 1993), (Haver and Winterstein, 2009). Contours may be obtained using different methods, such as the inverse first-order reliability method (IFORM), the inverse second-order reliability method (ISORM), the highest density contour method (HDC) or Monte Carlo simulations (Winterstein et al., 1993), (Chai and Leira, 2018; Haselsteiner et al., 2017; Bang Huseby et al., 2013). Applications of the ECM have been extensively covered in the marine technology and wind energy industries, where researchers have used the method to determine the design loads of offshore platforms within a probabilistic framework (Naess and Moan, 2012; Moan et al., 2005; Saranyasoontorn and Manuel, 2004, 2006; van de Lindt and Niedzwecki, 1997; Niedzwecki et al., 1998; Vanem, 2019; Montes-Iturrizaga and Heredia-Zavoni, 2015; Heredia-Zavoni and Montes-Iturrizaga, 2019; Moriarty et al., 2002; Fitzwater et al., 2003; Raed et al., 2020; Karmakar et al., 2016; Velarde

Abbreviations: ECM, Environmental Contour Method; IFORM, Inverse First Order Reliability Method; CDF, Cumulative Distribution Function.

* Corresponding author.
E-mail addresses: dario.r.f.castellon@ntnu.no (D.F. Castellon), aksel.fenerci@ntnu.no (A. Fenerci), ole.oiseth@ntnu.no (O. Øiseth).

https://doi.org/10.1016/j.jweia.2022.104943
Received 23 June 2021; Received in revised form 25 January 2022; Accepted 16 February 2022
Available online 2 April 2022

et al., 2019). Environmental contours have also been used to characterize the seismic hazard and derive the seismic design response spectra (Bazzurro et al., 1996; Van De Lindt and Niedzwecki, 2000; Loth and Baker, 2015). However, in design against wind actions on long-span bridges, the method remains largely unexplored despite the remarkable potential advantages.

Recently, Lystad et al. (2020) showed environmental contours for the Hardanger Bridge site based on a probabilistic wind field model from Fenerci and Øiseth (2018a) which was based on wind measurements on an existing bridge (Lystad et al., 2018). The results obtained for the Hardanger Bridge showed weaknesses in the current design methodology and motivated extension of the ECM to the structural design of new bridge sites. However, an obvious challenge that arises in the design of new bridges is obtaining data that are representative of extreme wind conditions because extreme wind conditions are inferred from measurement campaigns of relatively short duration. Additionally, wind measurements for new bridges are performed at meteorological stations in the vicinity of the site, instead of the midspan of the bridge, where the conditions are most relevant for bridge design. Here, we will attempt to extend the methodology to a new bridge site in complex terrain.

This paper presents environmental contours for the Sulafjord Bridge site to investigate the potential application of the ECM in the design of long-span bridges. Contours were obtained from the joint probability distribution of the mean wind speed, turbulence intensities and turbulence spectral parameters for each incoming wind direction. The joint turbulence model was established with a novel strategy where data from the 4-year mast measurement campaign (Furevik et al., 2020) and 10-year hindcast mesoscale simulations are combined, exploiting the advantages of both datasets. The contours represent the extreme wind fields for 4-, 50- and 100-year return periods.

This paper is outlined as follows. Section 2 presents the bridge site, measurement campaign, and hindcast data, including histograms of wind speed and direction, as well as the wind roses. This section expands the findings of the Sulafjord measurement campaign reported by Castellon et al. (Castellon, 2019) and Midjiyawa et al. (2021) and discusses how the dataset can be used to obtain the best possible wind field model for bridge design. Section 3 presents the proposed probabilistic modeling strategy, which is essentially a joint probability distribution of all the wind field parameters. The model is based on the joint lognormal distribution for turbulence intensities and turbulence spectral parameters that are dependent on the mean wind speed and direction. A Weibull distribution is used for the mean wind speed, and a discrete division for the mean wind direction is assumed. Section 4 presents the environmental contour lines for 4-, 50- and 100-year return periods and contour surfaces for a 100-year return period. The contour lines give combinations of two environmental parameters, while the surfaces correspond to combinations of three parameters. The four-year return period corresponds to the duration of the measurement period, whereas the results for 50- and 100-year return periods can be applied in bridge design. Section 5 presents the results and discusses the methodology's applicability to bridge design, including a comparison with reference values from the current design practice. Section 5 also contains modeling limitations and provides recommendations for future implementation of the ECM.

2. Wind conditions at the Sulafjord Bridge site

2.1. Bridge site

The Sulafjord is a Norwegian fjord located 10 km southwest of the city Ålesund on the western coast of Norway. The fjord is oriented from southeast to northwest, and it is approximately 12 km long, 4 km wide, and has a maximum water depth of 450 m. Fig. 1 shows the surroundings and the topography of the fjord, which is largely characterized by mountainous terrain with elevations of approximately 500 m on both sides, directing the wind flow through the fjord. Fig. 2 shows a picture of the fjord surroundings from the bridge location towards the north and south. Fig. 2 a) also shows the island Godøya, which is located on the northern side of the fjord. The island partly shields the fjord from the winds coming directly from the sea (Castellon, 2019). Fig. 3 shows an illustration of the Sulafjord suspension bridge adapted from illustrations by the Norwegian Public Roads Administration (NPRA) (Vegvesen, 2016).

2.2. Measurement campaign

Beginning in 2014, a wind measurement campaign led by the NPRA was deployed. This campaign aims to characterize the wind conditions in the Sula, Halsa and Vartdal fjords (Furevik et al., 2020). The data are handled by the Norwegian Meteorological Institute and are openly

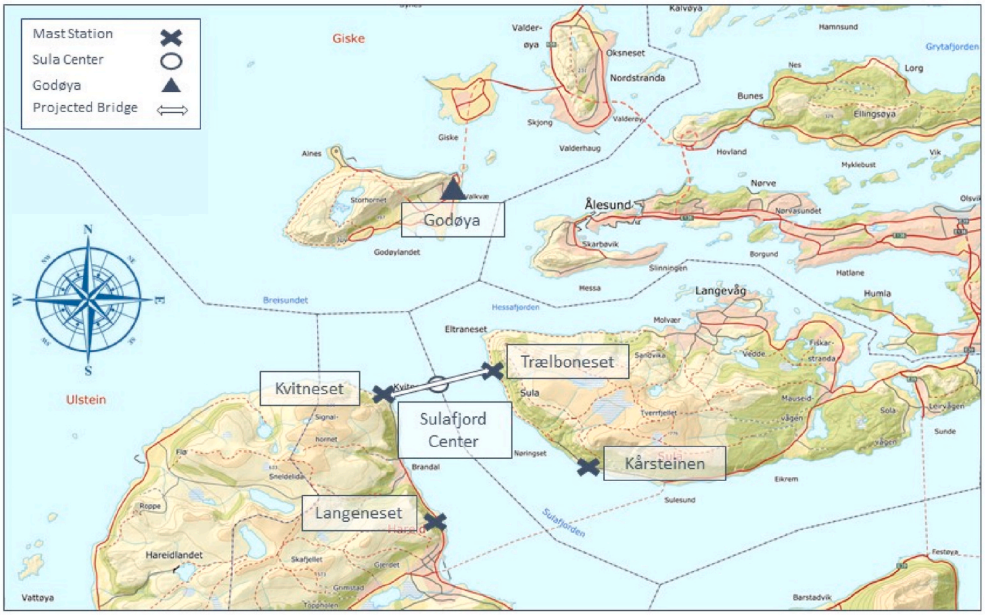

Fig. 1. Topographical map of the Sulafjord site (adapted from https://norgeskart.no/- ®norgeskart Norwegian Mapping Authority).

Fig. 2. The bridge site. (Images courtesy of NPRA).

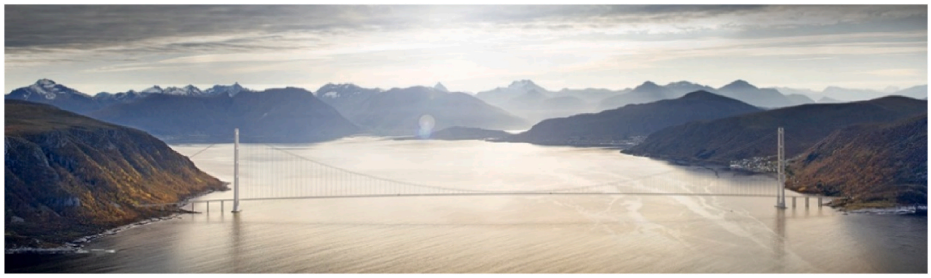

Fig. 3. Illustration of the Sulafjord suspension bridge. (Image courtesy of NPRA).

available (Norwegian Meteorological Institute, 2020). Four stations from the campaign are located at the Sulafjord site (cross symbols in Fig. 1), and Table 1 shows their geographical coordinates.

Each station is composed of a meteorological mast. The masts are equipped with wind sensors at different heights, to capture the vertical wind profile. The WindMaster Pro 3-Axis anemometers (Gill Instruments Limited) were used which can measure wind gusts up to 65 m/s. The speed resolution is 0.01 m/s, and the direction resolution is 0.1°, while the accuracy at 12 m/s is reportedly <1.5% RMS and 2° for speed and direction, respectively. Table 1 also shows the number of sensors and their altitude with respect to the sea level for each station.

2.3. Wind data from meteorological masts

The measurement data were analyzed to develop a statistical model of the wind conditions at the site. In total, 151,505 10-min intervals from sensors at approximately 50 m above sea level were analyzed. This elevation corresponds to the lowest sensor at Kvitneset and the second lowest at the other stations and most representative of the bridge height. Recordings with anomalies such as system log-out or missing data, within the averaging period of 10-min, are disregarded from the analysis as they cause irregularities in the power spectrum estimation. Further details of data processing are explained in section 2.3.3.

Table 1
Sulafjord wind mast station coordinates.

Station name	Latitude	Longitude	Sensors	Altitude (m)
Kvitneset	62°25′17.74"N	6° 0′4.03"E	3	92.5-71.5-44.5
Trælboneset	62°25′39.47"N	6° 3′45.45"E	3	76.8-48.3-27.3
Langeneset	62°23′10.68"N	6° 1′52.72"E	4	94.8-75-50-27
Kårsteinen	62°24′0.48"N	6° 7′9.82"E	3	62.8-40-13.4

The wind data are given in polar coordinates and need to be transformed to a Cartesian coordinate system aligned with the 10-min mean wind direction.

$$\begin{aligned} V + \ u(t) &= V_p(t)cos\{\varphi(t) - \overline{\varphi}\} \\ v(t) &= V_p(t)sin\{\varphi(t) - \overline{\varphi}\} \\ w(t) &= W(t) - \overline{W} \end{aligned} \tag{1}$$

Equation (1) shows the transformation of the wind velocity in polar coordinates with the magnitude $V_p(t)$ and direction $\varphi(t)$ into mean wind speed V and mean wind direction $\overline{\varphi}$ and the wind turbulence decomposition into along-wind $u(t)$, cross-wind $v(t)$ and vertical $w(t)$ components. Recordings with a mean speed below 5 m/s were discarded from the analyses as such records tend to be severely nonstationary due to rapid changes in temperature and wind direction. Such data can however be disregarded as they won't cause significant structural responses

and therefore not relevant for the application here, which is focused on extreme wind fields. Fig. 4 shows the histograms of the mean wind direction, $\overline{\varphi}$, from the mast-measurements where the north is aligned with zero. The histograms show clusters of samples at specific directions which are mainly governed by the terrain's topography. The cutoff-directions of the clusters were chosen corresponding to the peaks of the histograms. The figures show that there are two main directions at Trælboneset, Langeneset and Kåresteinen, while there are three directions at Kvitneset. The main directions were divided into these sectors such that wind recordings from different topographical conditions could be studied separately. The main directions are shown by dashed lines in the histograms and Table 2 reports their directional intervals. Trælboneset station shows the dominant cluster in the incoming direction interval 100°–230°. Further details about the topographic influence over the mentioned behavior was explored with the wind rose diagrams that will be presented in next section.

2.3.1. Wind roses

Fig. 5 shows wind roses of the stations' mean wind speeds on top of the topographical map. The map clearly illustrates that there are tall mountains close to the masts and that the terrain by the masts will influence the wind recordings severely for some directions. It is therefore not straightforward to compare the wind roses at the four masts. The wind roses at Trælbonset and Kvitneset shows that the main incoming wind direction is from south in both locations. This behavior can be explained by the island Godøya (Fig. 1), which partially shields the two locations from winds coming from the open sea. A similar pattern would normally be expected at Kåresteinen and Langeneset due to their close location. Nonetheless, their wind roses are significantly different. The mast at Langeneset is partly shielded from winds approaching from southwest by the tall mountain close by. Similarly, the winds coming from south are severely obstructed by the tall mountain behind the mast at Kåresteinen. This illustrates that the measurements gathered at Langeneset and Kåresteinen are not entirely representative for the southerly winds at a potential bridge crossing between Kvitneset and Trælboneset. The wind roses also illustrate that the wind field is shaped by the mountains along the fjord since the main wind directions tend to be aligned with the tall mountain sides for some of the wind directions. It should also be noted that the shape of the wind roses strongly depends on how many sectors that are used.

Table 2
Main directional sectors.

Location	Sector 1	Sector 2	Sector 3
Kvitneset	100°–230°	260°–360°	370°–410°
Trælboneset	120°–230°	280°–400°	–
Kårsteinen	90°–150°	220°–340°	–
Langeneset	80°–240°	290°–360°	–

According to the feasibility studies by the NPRA (Vegvesen, 2016), the most convenient track for a suspension bridge crossing the fjord will be near the Kvitneset and Trælboneset stations (thick line in Fig. 1). Fig. 6 and Fig. 7 show the histograms of the mean wind speed at both locations considering the directional division. Fig. 6 from Kvitneset shows sector 2 (250°–320°) as the dominant sector with the highest recorded mean wind speed and sector 1 (120°–210°) as the most populated sector with largest number of samples. Fig. 7 shows Trælboneset sector 1 as both dominant and most populated. The histograms and wind roses show that the winds coming from the seaside have lower mean wind speeds at Trælboneset station compared to other stations. The main reason for this behavior is the effect of the Godøya island which protects the Trælboneset-side of the track from the open sea winds while the Kvitneset-side is partially uncovered from northwestern sea winds. Evidence of this is clearly found from the Kvitneset recordings in which the maximum mean wind speed of 25.7 m/s was observed in the sector not protected by Godøya. The shielding effect also implies that the most critical wind conditions on the Sulafjord bridge are expected to come from the southern direction approaching nearly perpendicular to the bridge deck. The measurements gathered at Trælboneset are clearly most representative for the southerly winds approaching the bridge crossing since the southerly winds approaching Kvitneset has passed over a mountain close by. The data from Trælboneset is therefore used to

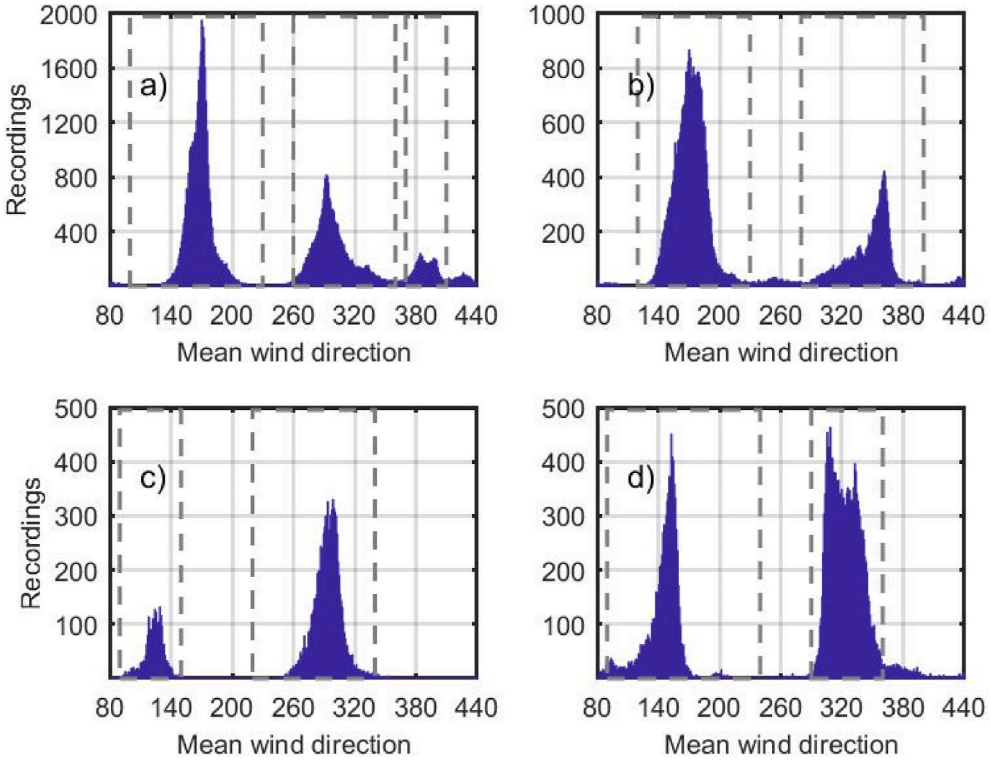

Fig. 4. Direction histogram station: a) Kvitneset b) Trælbodneset c) Kårsteinen d) Langeneset.

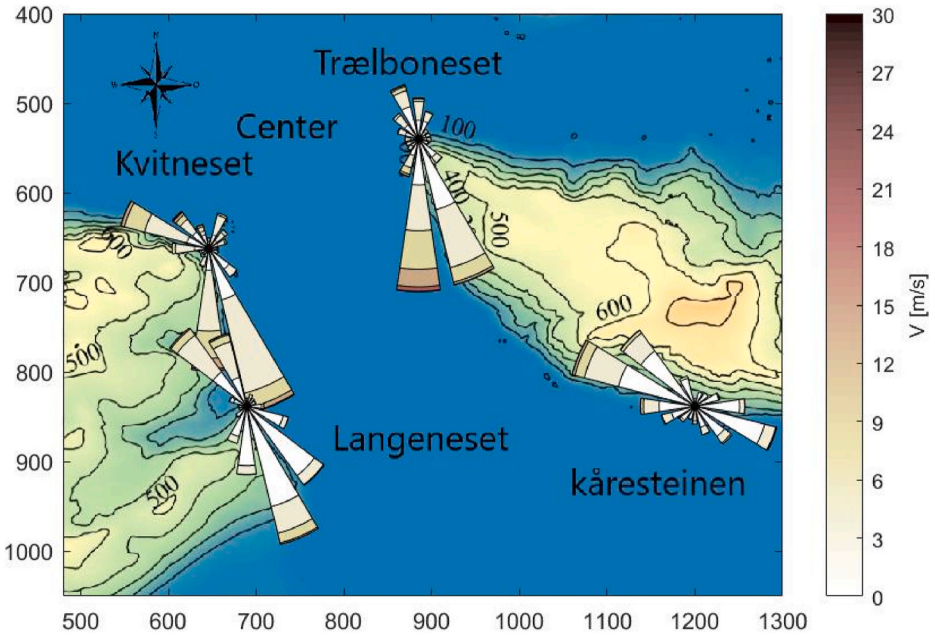

Fig. 5. Wind rose plot mean speed.

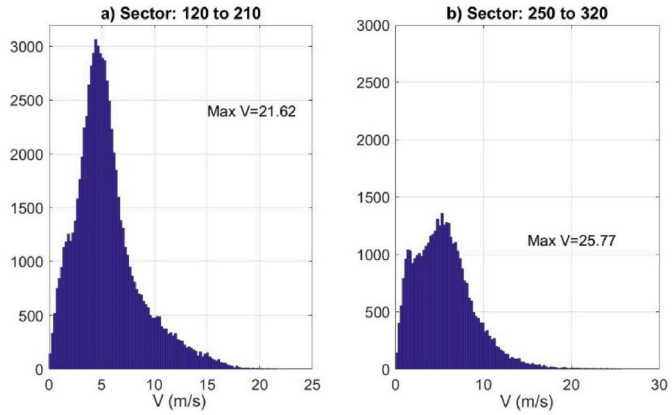

Fig. 6. Mean wind speed histograms for the Kvitneset station from measured data at a) Sector 1 b) Sector 2.

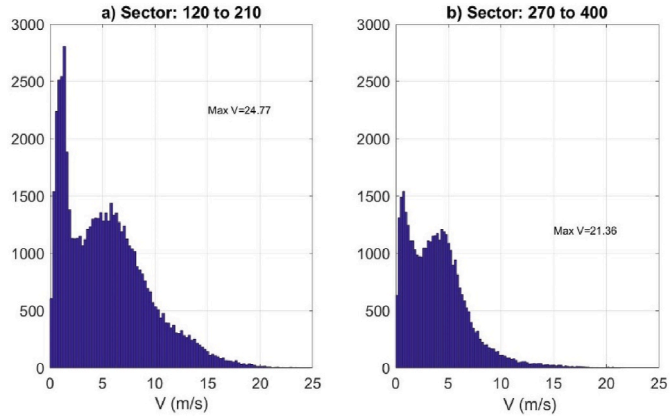

Fig. 7. Mean wind speed histograms for the Trælboneset station from measured data at a) Sector 1 b) Sector 2.

obtain the results presented in this paper.

2.3.2. Data processing

The recordings were resampled at 2 Hz to remove high-frequency content associated with possible vibration of the mast. The resampling does not introduce any significant inaccuracies since the wind characteristics will be applied in the design of a long-span bridge. In these types of projects the responses and associated load effects are dominated by vibration modes with natural frequencies much lower than 1 Hz. In addition, high-pass filtering was used to subtract nonstationary trends, as this technique better removes the variances in ramp-like events in the recordings (Hannesdóttir et al., 2019) than detrending each 10 min segment. The filter was a minimum-order, linear-phase, finite impulse response (FIR) with pass frequency $f_{pass} = 1/300\ hz$, steepness $s = 0.85$ and transition width $W = 5x10 - 4$, following the recommendations in (Hannesdóttir et al., 2019).

2.3.3. One-point turbulence spectrum

The turbulence was modeled from its one-point Kaimal-type power spectrum S_n, Equation (2) (Kaimal et al., 1972). Model uncertainties were introduced by assuming the mean wind speed (V), the along-wind, cross-wind and vertical turbulence intensities (I_u, I_v, I_w), and the spectral parameters (A_u, A_v, A_w) as stochastic variables. Despite the Kaimal-type power spectrum don't consider turbulence length scales in its formulation, the spectral parameters (A_u, A_v, A_w) are proportional and analogous to these quantities (Fenerci et al., 2017), (Fenerci and Øiseth, 2017). Parameters such the spatial coherence and the wind angle of attack are outside the capabilities of the measurement system because of the long distance between stations and the absence of an appropriate structural reference frame crossing the fjord site. In a design situation, uncertainties in those parameters can be modeled after measurements at similar sites, in the case of absence of such data.

$$\frac{S_n f}{(V I_n)^2} = \frac{A_n f_{z_h}}{\left(1 + 1.5 A_n f_{z_h}\right)^{5/3}},\ f_z = \frac{z_h f}{V},\ I_n = \frac{\sigma_n}{V} \tag{2}$$

The subscripts $n \in \{u, v, w\}$ indicate the along-wind and vertical turbulence components, z_h is the reference height, f is the frequency and σ_n represents the standard deviations.

For the estimation of the spectral parameters (A_u, A_v, A_w), the power spectral density function (PSD) of the turbulence components was ob-

tained by applying the Welch method, taking the average of 8 segments with a 50% overlapping and Hamming window. Then, the power spectra S_n from Equation (2) were fitted to the spectral parameters (A_u, A_v, A_w) in the least square sense. As an illustration, overlapping fitted and measured power spectra from a recording registered on 01.01.19 at Trælboneset station from 14:40 to 14:50 corresponding to the annual highest mean speed are shown in Fig. 8. Scatter in the measured PSD comes from the spectral estimation. The spectra have been estimated using the Welch method. Smoother estimates can be obtained using shorter windows, but this comes at the price of lower resolution and higher bias. The presented estimates provide a balance between scatter (variance) and bias & resolution of the estimate. The distributions of the (A_u, A_v, A_w) coefficients are not very sensitive to the applied settings in the spectral estimate when least squares are used to fit the model. Along with the spectral fittings of Fig. 8, Fig. 9 shows the time-histories of the turbulence components on the same interval. The time-histories show a stationary behavior. The figure also includes the time-history of the vertical angle of attack (β), which is a parameter of paramount importance for the bridge's non-linear aerodynamic behavior. The time-series of the angle of attack show that this value oscillates between −15 and 20°, this range is slightly higher than that reported on the Hardanger bridge (Barni et al., 2021). In contrast, the mean values of the vertical angle of attack shown in Fig. 10 respect to the mean wind speed correspond to observations of the Hardanger bridge (Fenerci and Øiseth, 2017). Thus, suggesting that the angle of attack at the Sulafjord bridge may have higher variation than at the latter location. To determine the actual effect of this parameter over the Sulafjord bridge, a complete study of the aerodynamic derivatives is required, however, such study is outside the scope of this paper. Nonetheless, with the probabilistic modeling provided here, it is possible to reproduce the vertical angle of attack for practical engineering applications, since for such cases, the vertical angle of attack is handled with simulated time-series depending on the spectral densities and the mean wind conditions.

2.4. Hindcast wind data

In addition to the mast measurement data, hindcast simulations were performed by Kjeller Vindteknikk (Vindteknikk and og Vartdalsfjorden, 2018). Simulated mean wind velocities were obtained using the state-of-the-art mesoscale numerical weather prediction system, the Weather Research and Forecast model (WRF) work version 3.2.1 (UCAR and, 2013), (Skamarocket al., 2008). The modeling structure, physical packages, numerical routines and other details are given in (Klemp et al., 2007), (Michalakeset al., 2001). The geographical input data in the model were adapted from the National Oceanic and Atmospheric Administration (NOAA) for the entire domain except for Norway and Sweden, where N50 land data from the Norwegian Map Authority and map data from the Geografiska Severgedata (GSD)-Land Cover were used. The meteorological input data were adapted from the European Center for Medium-range Weather Forecasting (ECMWF) using a resolution of approximate 0.7° and 6 h interval data as boundary of the model. The hindcast data are fitted to meteorological observations in the area using an assimilation model that incorporates all available observation globally into a numerical weather prediction model that creates a description of the state of the atmosphere on a uniform horizontal grid four times a day. The assimilation model incorporates data from several thousand ground based observation stations, vertical profiles from radiosondes, aircrafts, and satellites and are therefore reasonably accurate (Deeet al., 2011), (Berrisfordet al., 2009). The model was set up with 4 nested domains from which the inner domain has a resolution of 500 × 500 m (Fig. 11). This is the highest resolution possible as the simulations are limited to meso-scale and not to local topographical effects. The simulation model has 51 layers in the vertical with eight layers in the lower 200 m. The WRF-model computes the variation in the wind

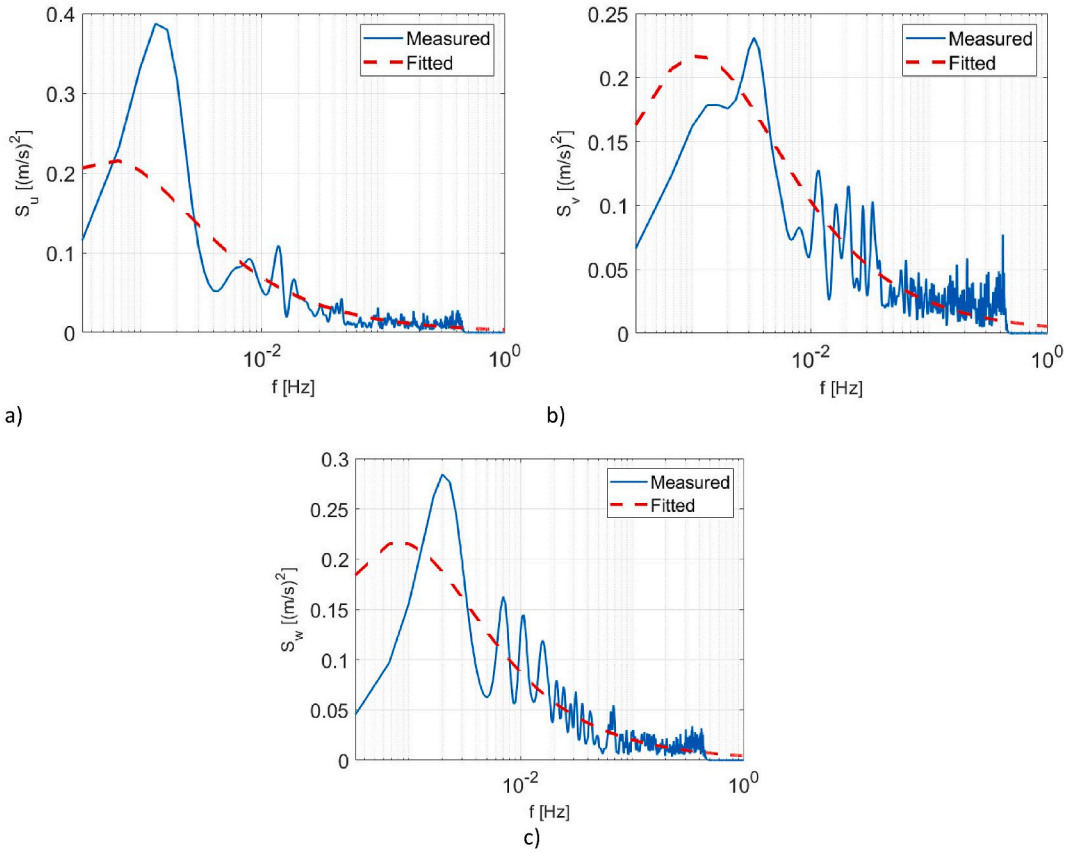

Fig. 8. Three components of the one-point spectrum 'max 2019' Record 01.01.19 from 14:40 to 14:50. a) Su b) Sv c) Sw.

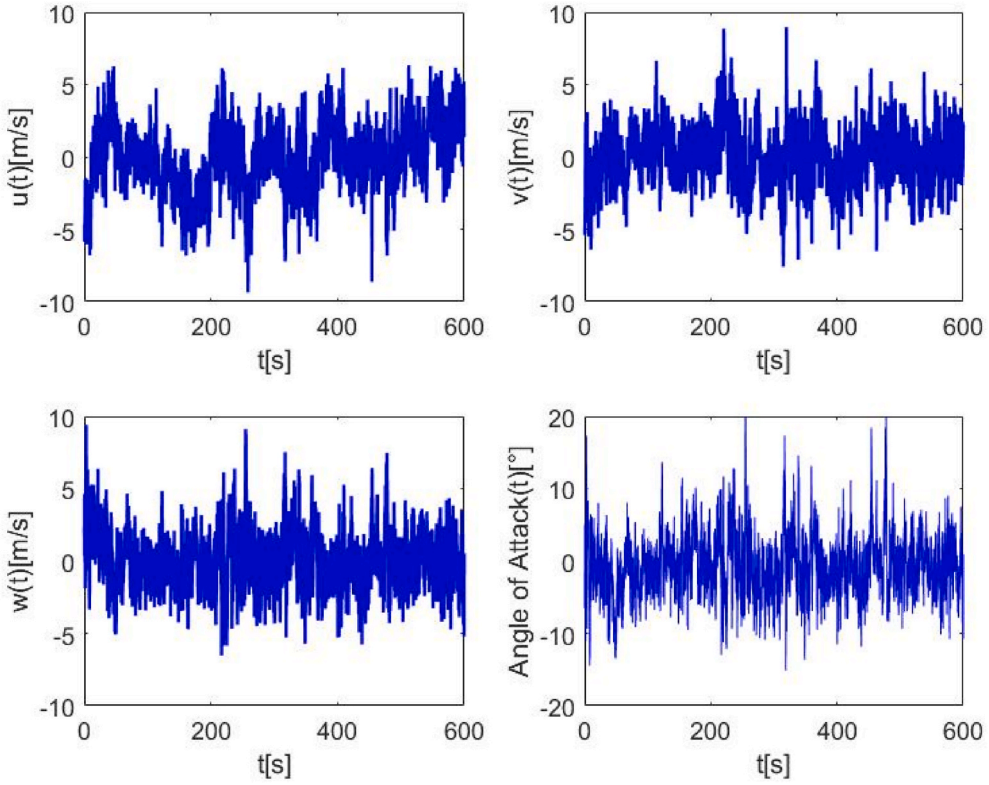

Fig. 9. Time-histories of the three components 'max 2019' Record 01.01.19 from 14:40 to 14:50. a) u b) v c) w d) angle of attack.

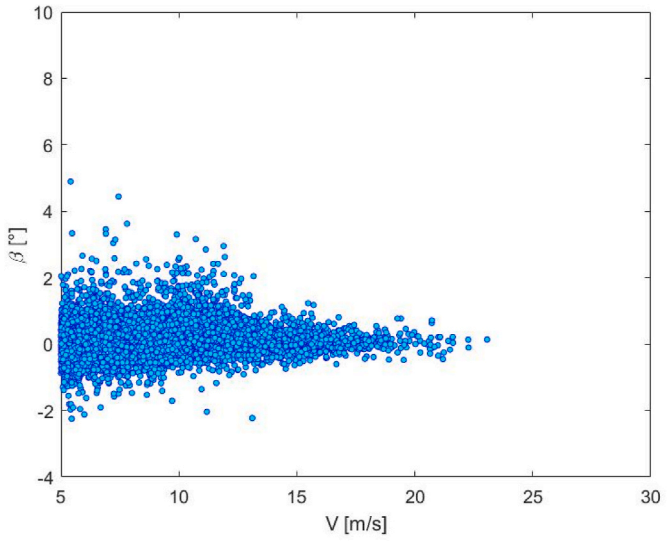

Fig. 10. Vertical angle of attack respect to mean wind speed.

conditions for a time step from 1 to 108 s in the different domains increasing the time step with decrease in the resolution, achieving then a more realistic temporal development of the wind conditions. Data is stores every 1 h of simulation. More information about the hindcast data set may be found in (Vindteknikk and og Vartdalsfjorden, 2018).

The simulated dataset is 10 years long starting from January 2007. The dataset contains the mean wind speed and direction for 1-h intervals in the locations of the four mast stations in addition to the Sulafjord center (62°25′19.68"N, 6°01′52.68"E) (circle in Fig. 1). The simulations were carried out at 10, 50, 70 and 100 m above the ground or water level. Histograms of the 1-h direction distribution for the different sites are presented in Fig. 12, while the principal sectors are reported in

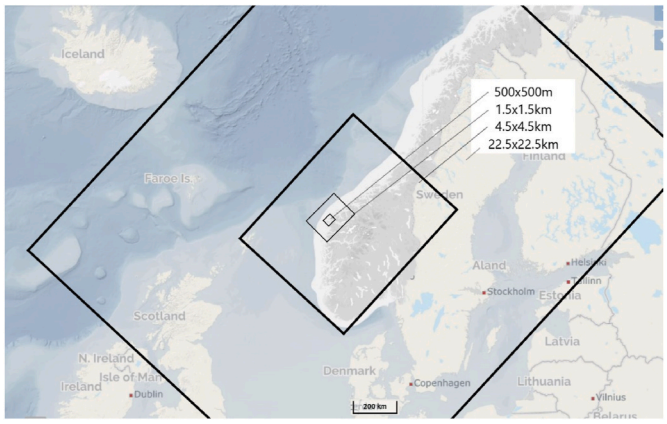

Fig. 11. Nested domains of hindcast dataset simulations (adapted from https://norgeskart.no/- ®norgeskart Norwegian Mapping Authority).

Table 3. The figure shows a similar trend in the distribution peaks as the site measurements. However, an increased scatter of samples towards the distribution valleys may be observed, with the most severe situation for the Kårsteinen station in which the peaks can barely be differentiated from the valleys. Validation of the hindcast data is presented in (Vindteknikk and og Vartdalsfjorden, 2018).

Similar to the recorded data, the wind rose of the mean wind speed for the simulation sites is shown in Fig. 13. The analyzed data correspond to the simulations at a 50-m height since it represents the bridge height. Simulated samples below 5 m/s were disregarded from the plots. It is not expected that wind roses from Figs. 5 and 13 coincide exactly since the wind flow is affected by the local topographical effects not included in meso-scale simulations. Then, the differences between the wind roses of Kårsteinen and Langeneset are plausible, and hence the erection of several mast stations in the area. On the other hand, local

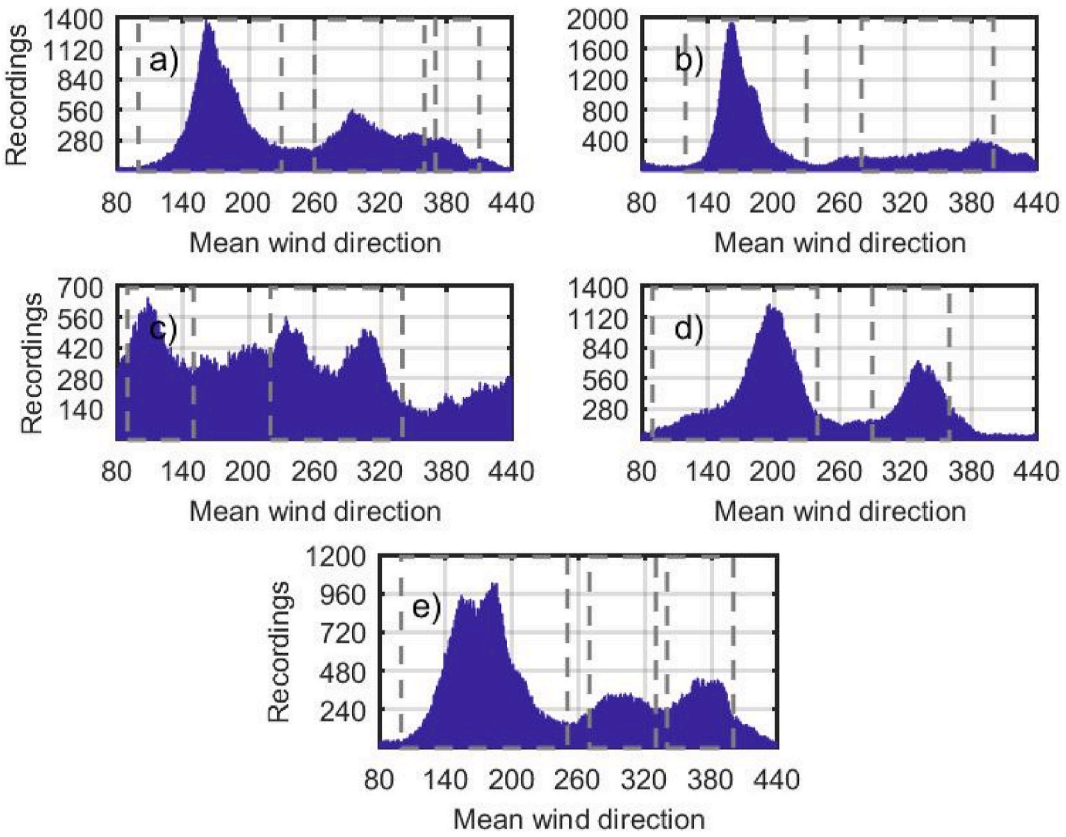

Fig. 12. Direction histogram from hindcast data locations: a) Kvitneset b) Trælbodneset c) Kårsteinen d) Langeneset e) Sulafjord center.

Table 3
Main directional sectors.

Location	Sector 1	Sector 2	Sector 3
Kvitneset	100°–230°	260°–360°	370°–410°
Trælboneset	120°–230°	280°–400°	–
Kårsteinen	90°–150°	220°–340°	–
Langeneset	80°–240°	290°–360°	–
Sulafjord center	100°-250	340°–400°	270°–330°

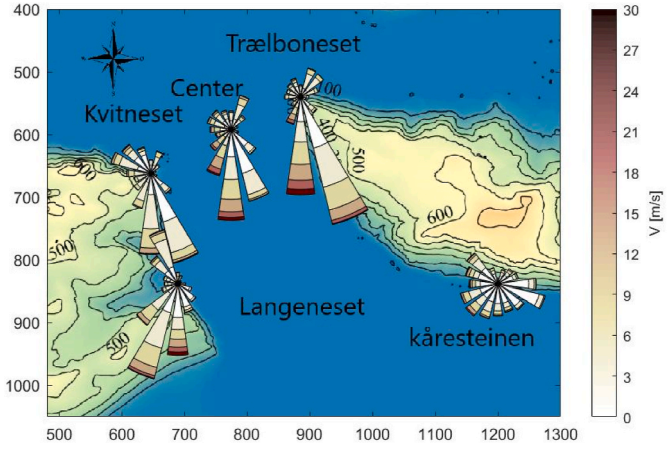

Fig. 13. Wind rose plot mean wind speed hindcast data.

topographical effects don't present a major complication at the Sulafjord center location, which is the most representative for the bridge and meso-scale simulations are still the best option for extreme mean wind velocity estimations because of their longer observation period.

2.4.1. *Wind speed histograms*

In a similar way as Figs. 6 and 7, Fig. 14 contains the histograms of the mean wind speed from Sulafjord center location but using the hindcast data. In this case the sector from 100° to 250° is both the dominant and most populated sector.

3. A probabilistic model of the wind field

A probabilistic model of the wind field is defined by a joint distri-

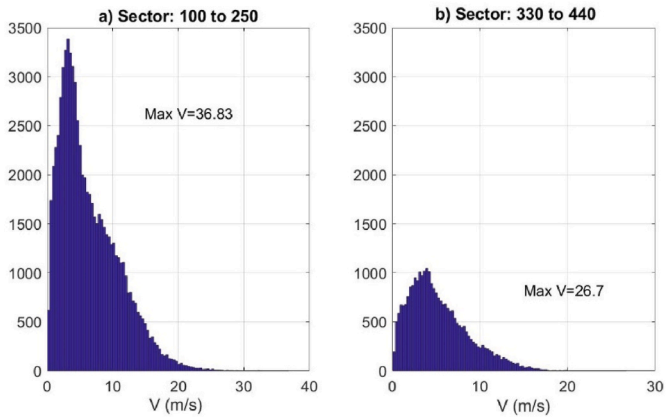

Fig. 14. Mean wind speed histograms of the Sulafjord center station from hindcast data at a) Sector 1 b) Sector 2.

bution of the turbulence parameters (Fenerci and Øiseth, 2018), (Lystad et al., 2020). Introducing W as the wind state variable collecting the wind parameters, its joint distribution can be expressed as the product of the conditional distributions:

$$F_W(W) = F_V(V)*F_{I_u,I_v,I_w,A_u,A_v,A_w|V}\,(I_u,I_v,I_w,A_u,A_v,A_w|V)$$
$$W = [\,V,\ I_u,I_v,I_w,A_u,A_v,A_w] \tag{3}$$

Fenerci et al. (2018) showed that the joint distribution can be expressed as the product of Weibull distribution of the mean wind speed and a joint lognormal distribution of the turbulence parameters. This is highly advantageous because the relation between the turbulence parameters can be determined by the correlation of parameters only. Fenerci et al. (2018) showed that the joint lognormal distribution fits the turbulence data of the Hardanger bridge. Whereas Lystad et al. (2020) showed that the Weibull fits the mean wind speed data for the same project. Using a similar approach, in this chapter the parameters of Equation (3) will be derived for the Sulafjord site. Chapter 3.1 is devoted to the Weibull distribution of the mean wind speed and chapter 3.2 to the joint lognormal distribution of the turbulence.

Measured data was not available at the fjord center and meso-scale simulations don't include turbulence effects. Therefore, a strategy combing both sources was implemented. The Weibull distribution of the mean wind speed was obtained using the meso-scale data as it covers a more extended period than the site measurements and it is possible to obtain the data at the desired midspan location. Subsequently, the joint lognormal distribution of turbulence parameters was obtained from the site anemometry measurements as the turbulence characteristics cannot be obtained from meso-scale simulations. However, as site measurements are not available at the fjord midspan, the turbulence parameters were assumed to be reasonably well represented by the measurements at the Trælboneset station. This follows both from simple considerations of the site topography (local effects are less expected) and the fact that the wind direction of the station matches the mesoscale simulations with good accuracy. Complementary arguments to the selection of Trælboneset station are discussed in section 3.2.

3.1. Mean wind speed distribution

The wind roses and wind histogram analysis showed that local topographical effects strongly influence the environmental variables. As discussed earlier, the dataset was split into sectors, where the dominant sector includes the recordings with the highest mean wind speeds. This information was further included in the probabilistic model by establishing the mean wind speed distribution from the dominant sectors at the Sulafjord center, $V = V|\overline{\varphi}_{dominant}$. The distribution for the mean wind speed F_V on Equation (3) is Weibull type with the following cumulative distribution function (CDF):

$$F_V(V) = 1 - \exp\left[\left(\frac{V}{\lambda}\right)^k\right];\ for\ V > 0 \tag{4}$$

With k *and* λ as the shape and scale parameters, respectively. The parameters were adapted from the hindcast data as it covers a more extended period than the site measurements and it is possible to obtain the data at the desired midspan location.

3.1.1. Extreme value distribution from hindcast data

Directly fitting the Weibull distribution from Equation (4) to the available data yields a good match with the central behavior of the distribution. However, the accuracy is lost in the tail where the largest wind loading conditions are expected. Thus, the parent distribution was established in correspondence to a type 1 generalized extreme value distribution (Gumbel) from the annual largest mean wind speeds, F_Z, reported in the hindcast data. In this way, most of the weight was given to fit the tail of the parent distribution.

$$F_Z(z) = 1 - \ e^{-e^{-y}},\ y = \frac{z-\alpha_1}{\alpha_2} \tag{5}$$

Here, α_1 *and* α_2 are the location and scale parameters of the distribution, respectively, y is the reduced variate, and z is a variable relative to the mean wind speed. A linear variation was assumed between y and the wind speeds following the best linear unbiased estimator (BLUE) method (Lieblein, 1974). Then, F_Z was established from the annual largest recordings ranked in ascending order, such that the lowest maximum has the rank of $m = 1$, and the highest rank is $m = n$, as follows:

$$F_z(z) = \left[\frac{m}{n+1}\right] \tag{6}$$

The distribution parameters α_1 *and* α_2, and thus F_z, are obtained by a least-squares fit from the reduced variate, which was directly adapted from the hindcast data.

$$y(z) = -\ln[-\ln(F_Z(z))] \tag{7}$$

Subsequently, F_V is established from F_Z utilizing the asymptotic theorem (Gumbel, 1958), i.e., F_V asymptotically approaches F_Z given that the number of short-term recordings in the one-year period, N, is sufficiently large and the statistical parameters of the individual recordings are independent. For the 1-h averaging period of the hindcast data, $N = 8760$ is sufficiently large to fulfil the requirement, and the parent distribution for the 1-h averaging period, $F_{V_{3600}}$, can be found as follows:

$$F_Z(V) = \left[F_{V_{3600}}(V)\right]^{N_{8760}} \leftrightarrow F_{V_{3600}}(V) = \left[F_Z(V)\right]^{1/N_{8760}} \tag{8}$$

A 10-min averaging period is typically used for structural design purposes, however the standard in meteorological forecast is 1-h intervals. Thus, a transformation between the averaging periods is required to proceed with the structural design. Direct conversion of averaging periods of mean wind speed records is not possible (Harper et al., 2009). Then, transformations must be completed on their estimates. In this work, the adjacent short-term 10-min intervals in the 1-h periods were assumed to be independent events allowing to estimate the parent distribution of the 10-min mean wind speed, $F_{V_{600}}$, as shown in Equation (9). This assumption doesn't involve a loss in accuracy given that the number of cycles of interest (10-min intervals in one year) is larger than the cut-off step-memory of stationary dependance (number of cycles in which the maximum events are no longer related), thus, the dependance between adjacent cycles is effectively negligible (Naess et al., 2013).

$$\left[F_{V_{3600}}(V)\right]^{N_{8760}} \cong \left[F_{V_{600}}(V)\right]^{6*N_{8760}} \leftrightarrow F_{V_{600}}(V) \cong \left[F_Z(V)\right]^{1/N_{52560}} \tag{9}$$

Fig. 15 a) shows the reduced variate for the recordings of the dominant wind direction (100°–250°) at the Sulafjord center, while Fig. 15 b) shows the associated annual Gumbel probability distribution. In both cases, the annual largest wind speeds are represented with circles. The velocities in the range of 25–35 are emphasized, as the design conditions are expected in the distribution's tail. Thus, the Weibull parent distribution establishment is focused on velocities from 25 to 35 m/s. Fig. 15 c) shows the scaled Gumbel CDF $\left[F_Z(V)\right]^{1/N_{52560}}$ in the continuous line and the fitted 10-min short-term Weibull CDF in the discontinuous line, $F_{V_{600}}$.

The parameters from the 10-min Weibull type parent distributions are shown in Table 4.

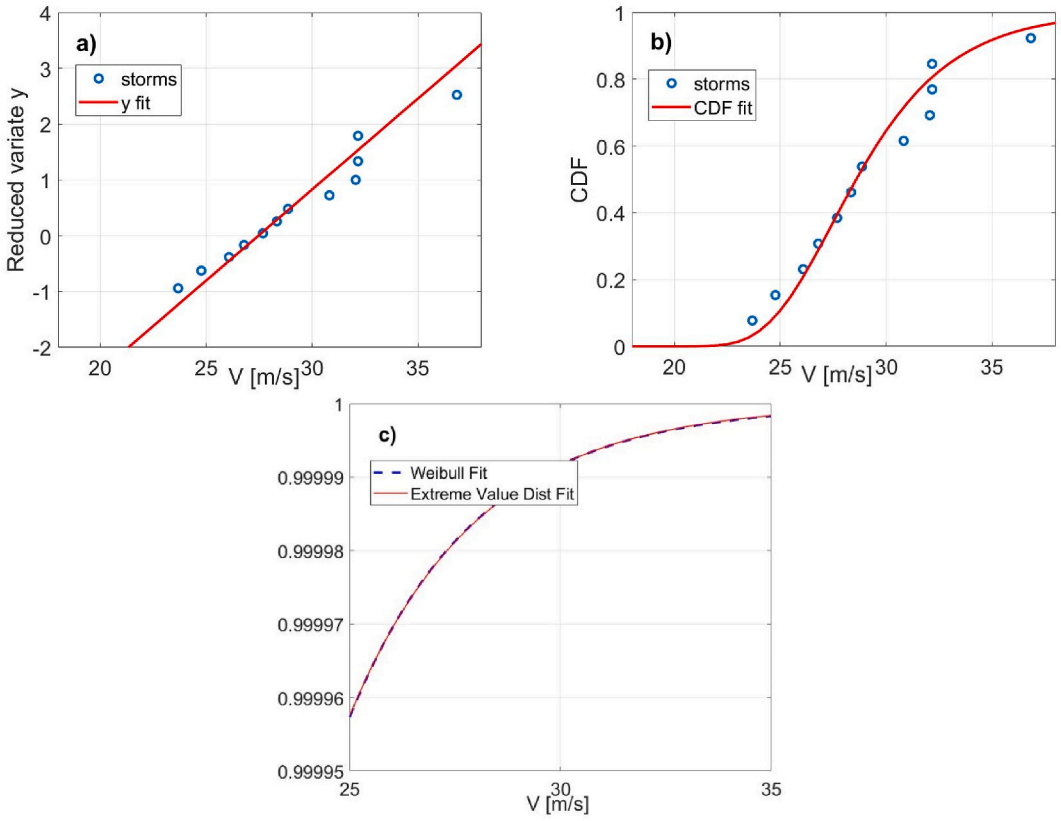

Fig. 15. Extreme distribution fit of the Sulafjord center from the hindcast data dominant sector a) Reduced variate b) Annual CDF c) 10-min CDF fitting.

Table 4
Parameters of the parent distributions from hindcast data for Eq. 3

Location	Sector	λ	k
Sulafjord center	100°–250°	1.52	0.82

3.2. Statistical properties of the turbulence parameters

Section 3.1 explained how to obtain the distribution for the mean wind speed. To complete the probabilistic model of Equation (3), This section explains how to obtain the joint distribution of the turbulence intensities (I_u, I_v, I_w) and spectral parameters (A_u, A_v, A_w), conditional to mean wind speed, $F_{I_u,I_v,I_w,A_u,A_v,A_w|V}$. Turbulence parameters are adapted from mast measurements according to the following procedure:

First, the data was divided in directional sectors from Table 2. Then, recordings with mean wind speeds below 11 m/s were disregarded from the analysis as attention is paid to the tail of the mean wind speed distribution. Subsequently, the data was divided depending on the mean wind speed in segments of 2 m/s, in this way trends of the joint distribution parameters respect to mean wind speed can be highlighted. On each segment of data, the parameters of the lognormal distribution and the correlation coefficients were fitted using the method of moments. Finally, the trends in the distribution and correlation parameters respect to the mean wind speed were fitted using least squares.

The size of the segments was chosen by engineering criterion. Small segments would leave few samples for distribution fitting whereas large segments would leave few points for trend fitting respect to mean wind speed. 2 m/s balanced the accuracy in both type of fittings given the number of recordings available.

The result is a joint lognormal distribution whose parameters are dependent of the mean wind speed. Parameters of a marginal lognormal distribution and correlation coefficients are described as follows:

$$
\begin{aligned}
&f_{logn}(x|\widetilde{\mu},\widetilde{\sigma}) = \frac{1}{x\widetilde{\sigma}\sqrt{2\pi}}\exp\left\{\frac{-(Ln\,x-\widetilde{\mu})^2}{2\widetilde{\sigma}^2}\right\}\\
&\widetilde{\mu} = \exp\left(\mu+\frac{\sigma^2}{2}\right),\ \widetilde{\sigma}^2 = \left[\exp(\sigma^2)-1\right]\exp(2\mu+\sigma^2)\\
&\rho(x,y) = \frac{1}{N-1}\sum_{i=1}^{N}\left(\frac{x_i-\mu_x}{\sigma_x}\right)\left(\frac{y_i-\mu_y}{\sigma_y}\right)\\
&\boldsymbol{R}_{xy} = \begin{bmatrix}1 & \rho(x,y)\\ \rho(y,x) & 1\end{bmatrix}
\end{aligned}
\tag{10}
$$

With, $f_{logn}(x|\widetilde{\mu},\widetilde{\sigma})$ the lognormal distribution a variable x and $\widetilde{\mu},\widetilde{\sigma}$ the lognormal mean and standard deviation (parameters of the distribution). $\rho(x,y)$, the correlation coefficient of the variables x *and* y, and $\boldsymbol{R}_{xy}$ the correlation matrix.

At middle of fjord there is not wind turbulence data. Therefore, turbulence conditions were adapted from the mast station that provided the most representative data. The wind roses from Figs. 5 and 13 show that most frequent and stronger winds for the fjord center come from the south and southwest and that this situation is also observed at Trælboneset. In addition, winds from south and southwest arrive mostly undistributed to Trælboneset making is suitable to represent the topographic conditions of the fjord center in these directions. Thus, the turbulence conditions at Trælbonset were used as the design conditions for the Sulafjord center.

Table 5
Number of samples at the interval division from measured data from the dominant sector at Trælboneset.

Speed interval	11–13	13–15	15–17	17-max
Samples	2681	1755	758	520

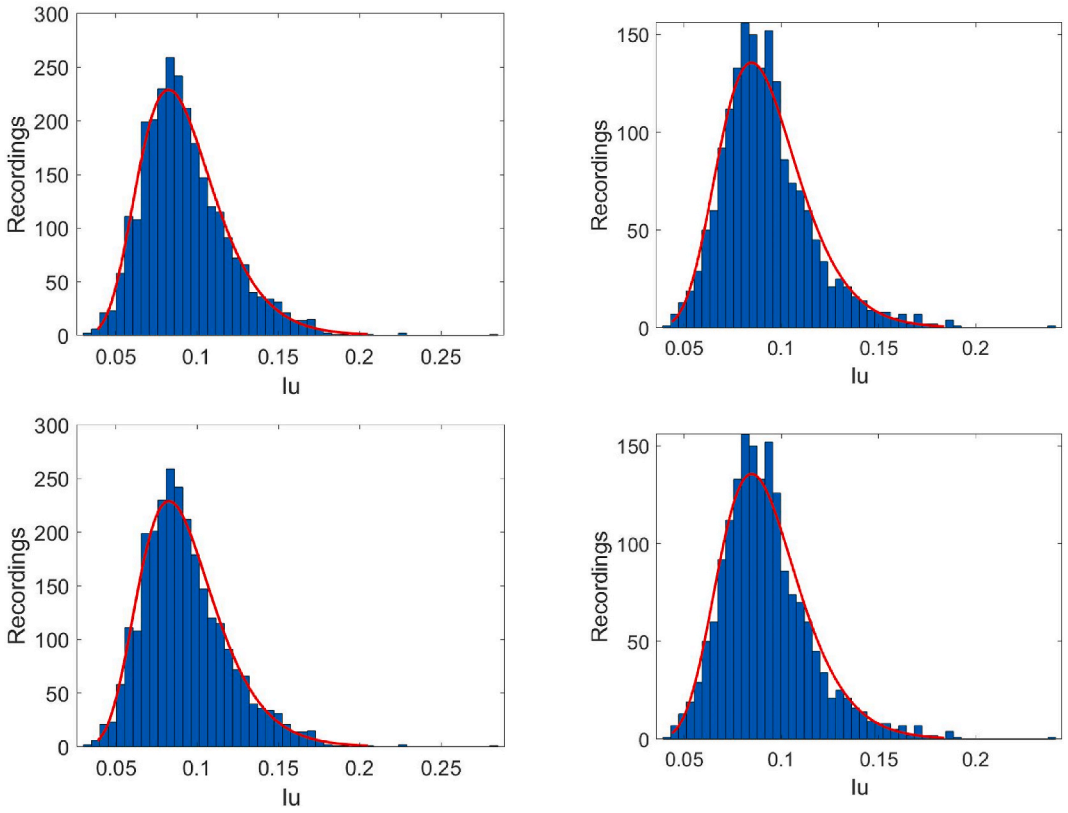

Fig. 16. Lognormal distributions for turbulence parameter I_u from the dominant sector at Trælboneset fitted at V = a) 11–13 m/s b) 13–15 m/s c) 15–17 m/s d) 17 m/s-max.

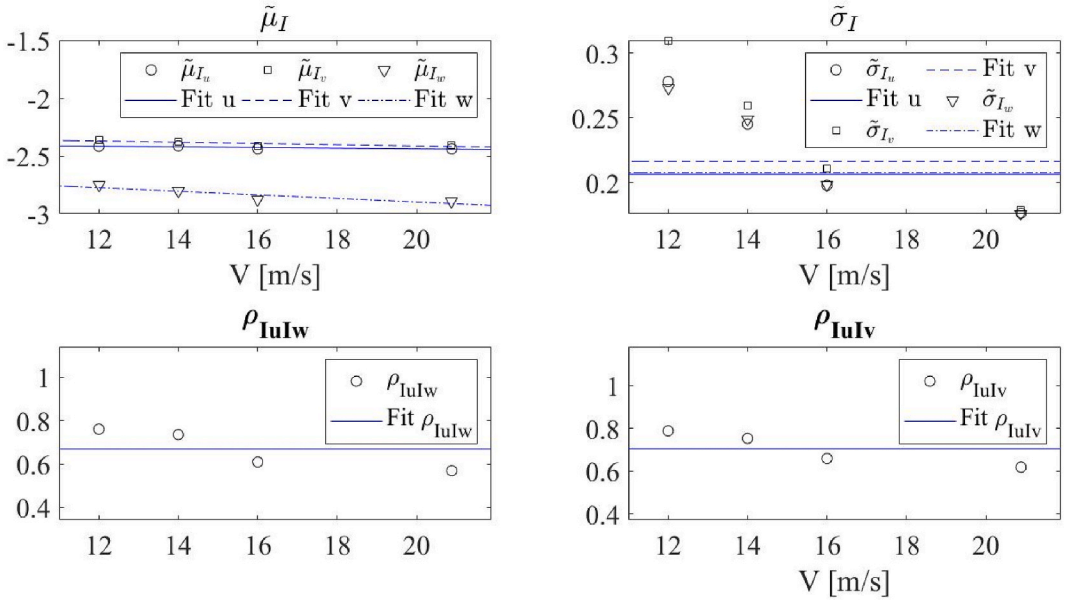

Fig. 17. Statistical parameter fit for the turbulence intensity: Lognormal parameter $\tilde{\mu}_I$, Lognormal parameter $\tilde{\sigma}_I$, Correlation coefficient $\rho_{I_uI_v}$, Correlation coefficient.$\rho_{I_uI_w}$

The number of samples in each discretization segment for the Trælboneset dominant sector (120°–230°) is reported in Table 5. As an example, Fig. 16 shows the lognormal distribution fittings for the I_u parameter for different mean wind speed segments on top of the histogram of the data.

Fig. 17 shows the variation in the lognormal distribution parameters of the spectral parameters $\tilde{\mu}_{A_i}$ and $\tilde{\sigma}_{A_i}$ with respect to the mean wind speed from Trælboneset dominant sector. Fig. 18 shows a similar plot for the turbulence intensity parameters $\tilde{\mu}_{I_i}$ and $\tilde{\sigma}_{I_i}$. $\tilde{\mu}_{A_i}$, $\tilde{\sigma}_{A_i}$ and the correlation coefficients are constant with respect to the mean wind speed, whereas $\tilde{\mu}_{I_i}$ shows a linear variation. The variation of $\tilde{\sigma}_{I_i}$, was adapted as constant despite it show a higher order trend. The reason behind this is that as less sampling points are present in the high mean wind speed

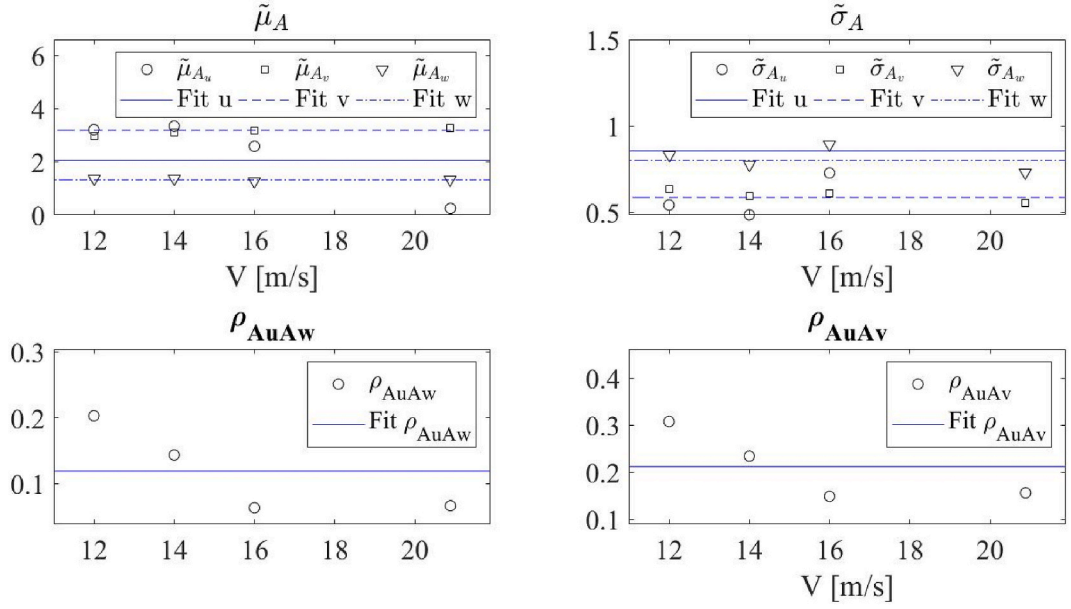

Fig. 18. Statistical parameters fit for the spectral quantities: Lognormal distribution parameter $\tilde{\mu}_A$, Lognormal distribution parameter $\tilde{\sigma}_A$, Correlation coefficient $\rho_{A_uA_v}$, Correlation coefficient.$\rho_{A_uA_w}$

Table 6
Statistical parameters of the turbulence model.

	$\tilde{\mu}$	$\tilde{\sigma}$
I_u	$-2.381-0.003V$	0.206
I_v	$-2.307-0.005V$	0.216
I_w	$-2.588-0.015V$	0.208
A_u	2.054	0.855
A_v	3.184	0.584
A_w	1.314	0.800

Table 7
Correlation coefficient fit matrix of the turbulence model.

	I_u	I_v	I_w	A_u	A_v	A_w
I_u	1.00					
I_v	0.71	1.00		Symmetric		
I_w	0.67	0.70	1.00			
A_u	0.00	0.00	0.00	1.00		
A_v	0.16	0.56	0.18	0.00	1.00	
A_w	0.00	0.00	0.47	0.00	0.19	1.00

range; this may lead to inaccuracies in the dispersion of the sample affecting the lognormal standard deviation. This effect is however more pronounced in the lognormal normal standard deviation than the lognormal mean, therefore, values of $\tilde{\mu}_{I_i}$ are still acceptable. This follows the recommendations found the literature (Fenerci and Øiseth, 2018), (Hannesdóttir et al., 2019). The values of the fitted parameters are reported in Table 6, while the correlation coefficient matrix is in Table 7. To simplify the modeling, correlation coefficients between −0.15 and 0.15 which are negligible for the calculations were not reported in the table.

4. Environmental contours

4.1. Environmental contour method

The established probabilistic model expresses the joint distribution of the correlated stochastic wind variables and provides the basis for obtaining the environmental contours. The ECM allows for the assessment of the model uncertainties considering multiple correlated stochastic variables. The method approximates the reliability integral based on an inverse application of the first-order reliability method (FORM) (Hasofer and Lind, 1974) (Winterstein et al., 1993):

$$p_e = P[g(\boldsymbol{X}) > 0] = \int_{g(\boldsymbol{X})>0} f_X(x)dx \tag{11}$$

where p_e is the exceedance probability of an extreme event, $\boldsymbol{X}$ $(\bar{\varphi}, V, I_u, I_v, I_w, A_u, A_v, A_w)$ is the set of stochastic variables and $g(\boldsymbol{X})$ is the limit function, which represents the difference between a generic wind condition $W(\boldsymbol{X})$ and the extreme wind condition W_{RP}, which is associated with the long-term extreme value of $\boldsymbol{X}$ with a return period *RP in years.* $g(\boldsymbol{X}) = W(\boldsymbol{X}) - W_{RP}$.

For design applications, the probability of exceedance is fixed to a design practice (or construction code) through the long-term return period *RP* in years. Thus, this value can be computed for the given return period in terms of short-term processes with T_{st} duration in minutes.

$$p_e = \left[\frac{RP \text{ x } 365.25 \text{ x24 x60}}{T_{st}}\right]^{-1} \tag{12}$$

The set of stochastic variables $\boldsymbol{X}$ is transformed into a set of independent normally distributed variables, $\boldsymbol{U}(u_1, u_2, \ldots, u_n)$, given that the proper transformation rule is reversible. A detailed explanation of the method and its advantages may be found in (Winterstein et al., 1993). In the transformed space, the shortest distance between the boundary of the limit function $(\tilde{g}(\boldsymbol{U}) = 0)$ and the origin is known as the reliability index, β. This parameter is fixed in correspondence to the exceedance probability and is computed by exploiting the symmetry of the joint standard normal cumulative distribution function, $\Phi(x)$:

$$\begin{aligned} p_e &\cong \Phi(\beta) \\ \beta &\cong -\Phi^{-1}(p_e) \end{aligned} \tag{13}$$

Although the boundary of the limit function can adopt complex shapes, it can reportedly be approximated by its first-order Taylor expansion (Hasofer and Lind, 1974). Then, an optimization procedure is applied as follows:

$$\text{Given } \beta : \text{find } W_{RP} = max|W(\boldsymbol{U})|; subjectto|\boldsymbol{U}| = \beta \tag{14}$$

The result is a hypersphere of radius β in the standard normal space

that shall be transformed back to the space of the original variables. Herein, two reversible transformation rules were applied because the mean wind speed and the turbulence structure follow different distribution types. The Weibull distributed mean wind speed was transformed with the Rosenblatt transform (Rosenblatt, 1952), while the correlated lognormal distributed turbulence parameters were transformed with a linear transform.

The Rosenblatt transformation works by obtaining the joint CDF from the product of the marginals:

$$F_{x1x2..xn}(x_1, x_2, \ldots, x_n) = F_{x1}(x_1)F_{x2}(x_2|x_1)\ldots F_{xn}(x_n|x_{n-1}\ldots.x\_1) \tag{15}$$

Then, the variables are transformed by considering the conditional distributions individually. The mean wind speed was chosen as the first variable, as it is considered the most important variable for the buffeting response of long-span bridges (Castellon et al., 2021). Then, the mean wind speed was transformed first.

$$F_V(V) = \Phi(u_1) \leftrightarrow \mathrm{V} = F_{\mathrm{V}}^{-1}[\Phi(u_1)] \tag{16}$$

When the stochastic variables are correlated and normally distributed, the linear transformation rule can be applied.

$$\begin{aligned} &\boldsymbol{U} = \boldsymbol{A}(\boldsymbol{X} - \boldsymbol{M}_X) \leftrightarrow \boldsymbol{X} = \boldsymbol{A}^{-1}\boldsymbol{U} + \boldsymbol{M}_X \\ &\boldsymbol{M}_X = \left[\mu_{x_1}\ \mu_{x_2}, \ldots,\ \mu_{x_n}\right] \end{aligned} \tag{17}$$

where A is a triangular matrix that can be found using the Cholesky decomposition of the covariance matrix C_{XX}, which is Hermitian and positive definite:

$$\boldsymbol{C}_{XX} = \boldsymbol{A}^{-1}\,\boldsymbol{A}^{-T} \tag{18}$$

with

$$\boldsymbol{C}_{XX} = \begin{bmatrix} \sigma_{x_1}^2 & \rho_{12}\sigma_{x_1}\sigma_{x_2} & \cdots & \rho_{1n}\sigma_{x_1}\sigma_{x_n} \\ \rho_{21}\sigma_{x_1}\sigma_{x_2} & \sigma_{x_2}^2 & \cdots & \rho_{2n}\sigma_{x_2}\sigma_{x_n} \\ \vdots & \vdots & \ddots & \vdots \\ \rho_{n1}\sigma_{x_1}\sigma_{x_n} & \rho_{n2}\sigma_{x_2}\sigma_{x_n} & \cdots & \sigma_{x_n}^2 \end{bmatrix} \tag{19}$$

Then, for the case in which stochastic variables are correlated and lognormally distributed, the same transformation rule procedure applies, and the lognormal variables can be found as follows:

$$\boldsymbol{X} = \exp\left(\boldsymbol{A}^{-1}\boldsymbol{U} + \boldsymbol{M}_X\right) \tag{20}$$

The full set of turbulence parameters conditional on the mean wind speed are transformed in a single operation using the linear transformation rule for the case of lognormal distributed variables from Equation (20).

$$F_{I_u,I_v,I_w,A_u,A_v,A_w|V}\ (I_u, I_v, I_w, A_u, A_v, A_w|V) = \Phi(u_2, u_3, u_4, u_5, u_6, u_7) \tag{21}$$

4.2. Sulafjord contours

4.2.1. Reference values from standard methodologies

The general practice in bridge design is to estimate the mean wind speed from an extreme value analysis and the turbulence variables from code values or measurements, usually dependent on the mean wind speed and the reference height. Reference values of the wind variables required for the Sulafjord bridge following the standard design methodology are reported in Table 8. The table presents mean wind speeds with 50- and 100-year return periods. Additionally, the table provides turbulence intensities (I_u, I_v, I_w) and spectral parameters (A_u,A_v, A_w) corresponding to their mean values for recordings above 15 m/s from the dominant incoming direction. Reference values of turbulence intensities and spectral parameters at the Sulafjord center were adopted from Trælbonset since site measurements are not available at the fjord center.

4.2.2. Design contours

The environmental contour lines for the Sulafjord bridge design for return periods of 4, 50 and 100 years are shown in Fig. 19. Site measurement data are also plotted along with the contour lines. The x-axis of the subfigures represents the mean wind speed, and the y-axis represents each of the remaining turbulence parameters. The 4-year contours represent the measurement campaign period and envelope the measured data well. Additionally, the 50- and 100-year return period contours represent extreme wind conditions. Reference values are reported in Table 8. Finally, contour surfaces for the 100-year return period of the turbulence intensity parameters are shown in Fig. 20.

5. Discussion

The results show that environmental contours successfully capture the variability in the site data. In general, the 4-year contours covered the measured data well. Furthermore, 50- and 100-year contours produce reasonable estimates of the extreme wind fields that follow the site data. Compared with the current design methodology, the contours represent a more complete description of the extreme wind fields, as they also include turbulence measurements. Therefore, presenting the extreme wind conditions of the Sulafjord Bridge site with environmental contours shows a significant advantage to the traditional wind speed method using the same resources typically available in the design of long-span bridges. Then, a designer will use the contours to identify combinations of environmental parameters that provide the largest response by checking points along the contour lines. The procedure is explained in (Lystad et al., 2020), (Lystad et al., 2021).

5.1. Model recommendations

Several challenges arise when developing contours based on probabilistic modeling with the proposed strategy for long-span bridge design. First, hindcast simulations are limited to the mesoscale, and site measurement campaigns have relatively short periods. Thus, the mean wind speed and turbulence parameters of probabilistic modeling should be established separately. Furthermore, locations with higher wind loads are often in the middle of the bridge's span, where site measurements from mast stations are rarely available. Additionally, establishing the joint distribution of the turbulence parameters requires approximations that are applicable beyond the range of available data. In the following section, the modeling limitations are discussed together with the strategies implemented to overcome these limitations.

First, there are discrepancies between the averaging period of the hindcast data and the site measurements. The hindcast data were simulated using a 1-h averaging period, whereas the site measurements used 10 min. It is recommended that the discrepancies between the averaging periods for the mean wind speed be resolved by considering the adjacent short-term 10-min intervals in 1 h as independent. This assumption yields conservative estimations of the mean speed values. The benefit from using data from the meso-scale model is that longer time series of mean wind speed are available and that data for mean wind speed is available at the middle of the fjord. Mast measurements is clearly the best alternative if many years of data in a representative

Table 8
Reference values from mean wind speed and turbulence parameters.

Parameter	V_{50}	V_{100}	I_u	I_v	I_w	A_u	A_v	A_w
Sulafjord Center	39.83	42.1	0.089	0.091	0.057	12.08	29.37	5.33

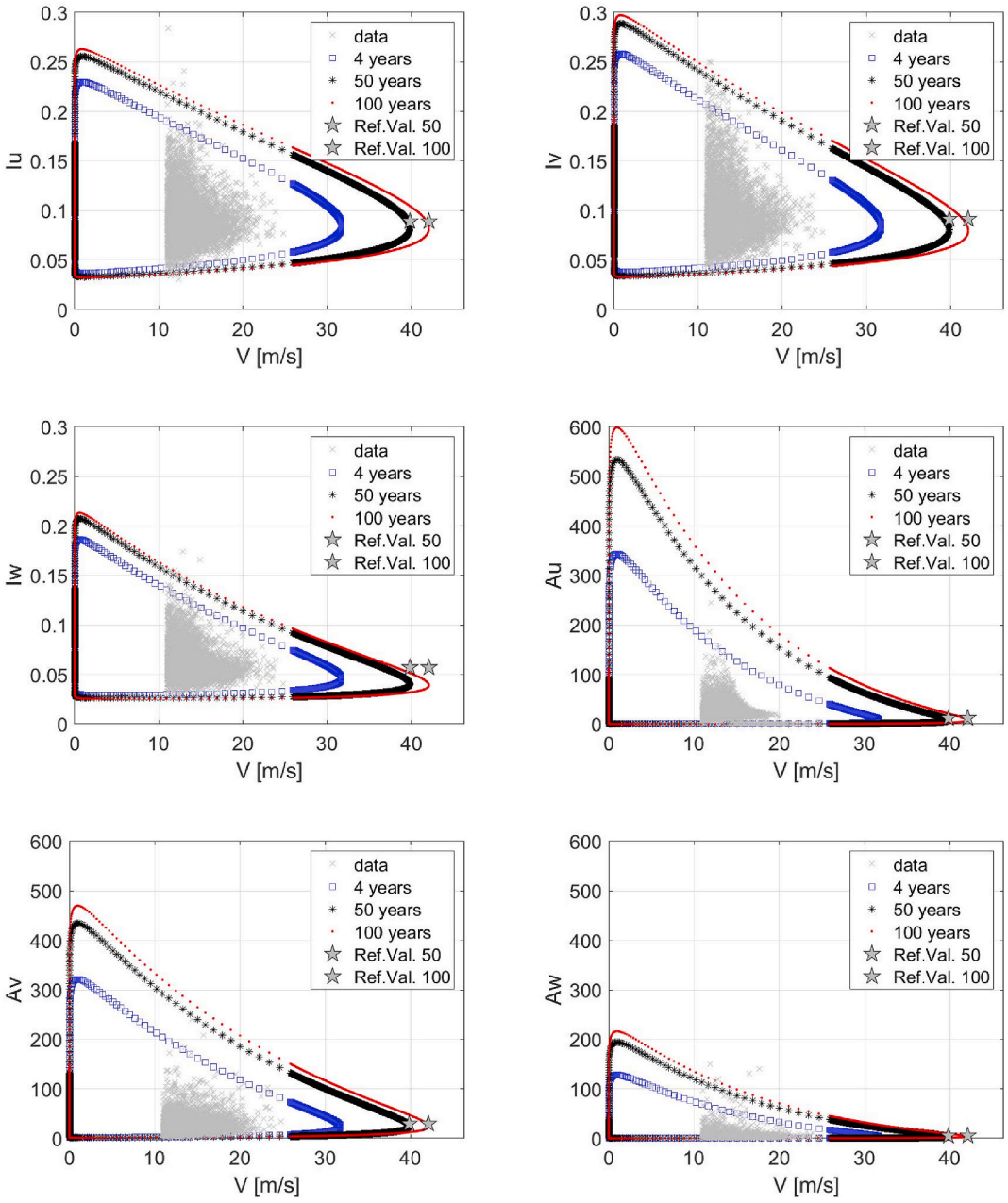

Fig. 19. Environmental contours of Sulafjord bridge design.

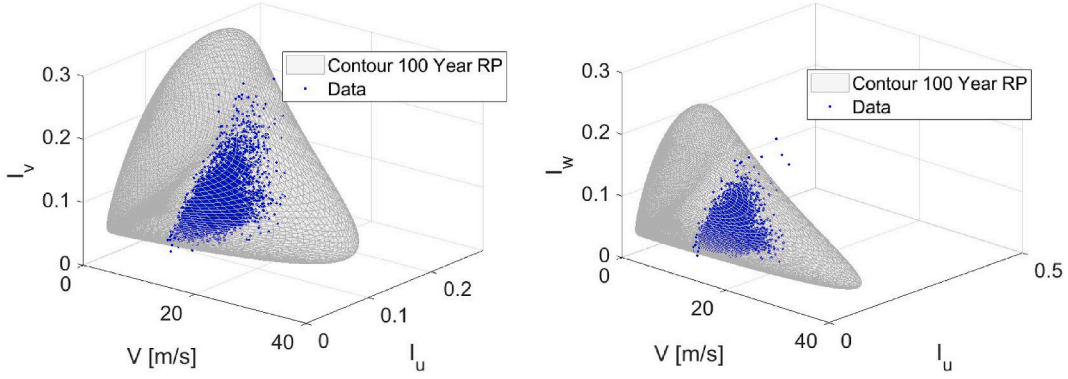

Fig. 20. Surface contours of the 100-year return period for Sulafjord bridge design: a) $I_u - I_v$ b). $I_u - I_w$

location at the bridge site is available. This is however rarely the case making meso-scale simulation an attractive alternative to cover longer time periods.

Additionally, site measurement data are not available at the center of Sulafjord, making it necessary to infer its turbulence properties from other available locations. Kårsteinen and Langeneset were not considered in the analysis because of their distant locations from the bridge track. The Kvitneset station could also be considered as a viable alternative, but it is seen that the winds at the midspan of the fjord does not follow the same direction as the winds at Kvitneset. The local topography around the station also suggests that local effects are likely to dominate the turbulence characteristics. On the other hand, Trælboneset station has almost twice the amount of strong wind records (above 17 m/s). Thus, it was decided to derive the turbulence model after Trælboneset records as it also contains a good number of records to ensure a good distribution fitting in the mean wind speed range above 10 m/s.

Finally, Figs. 17 and 18 show the variation in the joint distribution parameters with respect to the mean wind speed. All the correlation coefficients ρ_{ii} and the lognormal mean parameter of the turbulence intensity $\widetilde{\mu}_{I_i}$ agree with their adopted functions. Significant deviations can be observed between with the lognormal standard deviation parameter $\widetilde{\sigma}_{I_i}$ and its adopted constant value. The number of recordings decrease for higher mean wind speeds affecting the uncertainty in the distribution fittings with a stronger effect on the $\widetilde{\sigma}_{I_i}$ parameter compared to the $\widetilde{\mu}_{I_i}$ parameter. Then, trends of sigma may be attributed to lack of data, because using linear or higher order functions produce unrealistic estimates of the turbulence in the extrapolated region. Therefore, the constant vale of $\widetilde{\sigma}_{I_i}$ was chosen as it produced stable estimates. Similar approach may be found the literature (Fenerci and Øiseth, 2018), (Hannesdóttir et al., 2019).

6. Conclusion

In this paper, the wind conditions and wind characterization at the Sulafjord Bridge site from the 4-year mast measurement campaign and the 10-year hindcast simulation data are presented. A probabilistic model of the environmental variables was established using a novel and practical strategy in which hindcast simulations are combined with filed measurements. Efficient techniques for combining these datasets are an open matter of discussion and therefore were addressed in this study. The probabilistic model expresses the joint probability distributions of the turbulence intensities (I_u, I_v, I_w) and spectral parameters (A_u, A_v, A_w) conditional on the mean wind speed (V) and mean wind direction. The mean wind speed was modeled using a Weibull distribution transformed from the extreme value distribution of the hindcast data, where the mean wind direction was modeled as a discrete variable since the fjord distributes the flow in discrete directions. The joint distribution of the remaining wind variables (turbulence intensities and spectral parameters) were established from the site measurement data as a joint lognormal distribution with correlation coefficients.

Environmental contours were obtained for 4-, 50- and 100-year return periods based on the probabilistic turbulence model. The contours reasonably captured the variability in the wind conditions at the fjord site when compared with the site measurements. The contours present combinations of wind field parameters for the given return periods. As such, for instance wind conditions with higher turbulence intensities occurring at lower mean wind speeds can also be obtained and checked for design purposes. Therefore, designing the Sulafjord Bridge with the ECM will increase the accuracy in the extreme response predictions as opposed to the current practice. It is also concluded that the ECM uses the available data in a more efficient manner.

In conclusion, it is recommended to use the ECM to characterize the wind conditions at a bridge site using data typically available at the design stage of long-span bridges.

Data availability statement

Some or all data, models, or code used during the study were provided by a third party. Hindcast data from Kjeller Vindteknikk AS. Direct requests for these materials may be made to the provider as indicated in the Acknowledgements.

Some or all data, models, or code generated or used during the study are available in a repository online in accordance with funder data retention policies. Mast measurements (Norwegian Meteorological Institute, 2020).

CRediT authorship contribution statement

Dario Fernandez Castellon: Writing – original draft, Software, Methodology, Formal analysis. **Aksel Fenerci:** Writing – review & editing, Data curation, Investigation. **Ole Øiseth:** Conceptualization, Supervision, Project administration.

Declaration of competing interest

The authors declare that they have no known competing financial interests or personal relationships that could have appeared to influence the work reported in this paper.

Acknowledgments

The research presented in this paper was financially supported by the NPRA as a part of the E-39 Coastal highway project. The authors recognize the help from Kjeller Vindteknikk AS and Hálfdán Ágústsson for sharing the hindcast data and from the Norwegian Meteorological Institute for making the site measurement data available.

References

Bang Huseby, A., Vanem, E., Natvig, B., 2013. A new approach to environmental contours for ocean engineering applications based on direct Monte Carlo simulations. Ocean Eng 60, 124–135. https://doi.org/10.1016/j.oceaneng.2012.12.034.

Barni, N., Øiseth, O., Mannini, C., 2021. Time-variant self-excited force model based on 2D rational function approximation. J. Wind Eng. Ind. Aerod. 211, 104523. https://doi.org/10.1016/j.jweia.2021.104523.

Bazzurro, P., Winterstein, S.R., Ude, T.C., Cornell, C.A., 1996. Magnitude-distance contours for probabilistic seismic hazard analysis. Probabilistic Mech. Struct. Geotech. Reliab. Proc. Spec. Conf. 202–205. August 1996.

Berrisford, P., et al., 2009. The ERA-Interim Archive. ECMWF, Shinfield Park, Reading [Online]. Available: https://www.ecmwf.int/node/8173.

Castellon, D.F., 2019. Aksel Fenerci, and O. Øiseth, "A probabilistic analysis OF the wind field at SULAFJORDEN bridge SITe. In: ANCRiSST:14th International Workshop on Advanced Smart Materials and Smart Structures Technology, pp. 115–118. https://doi.org/10.13133/9788893771146 [Online]. Available:

Castellon, D.F., Fenerci, A., Øiseth, O., 2021. A comparative study of wind-induced dynamic response models of long-span bridges using artificial neural networks, support vector regression and buffeting theory. J. Wind Eng. Ind. Aerod. 209, 104484. https://doi.org/10.1016/j.jweia.2020.104484.

CEN, 2004. Eurocode 1: Actions on Structures - Part 1-4, 1. General actions - Wind actions.

Chai, W., Leira, B.J., 2018. Environmental contours based on inverse SORM. Mar. Struct. 60, 34–51. https://doi.org/10.1016/j.marstruc.2018.03.007. December 2017.

Ciampoli, M., Petrini, F., Augusti, G., 2011. Performance-based wind engineering: towards a general procedure. Struct. Saf. 33 (6), 367–378. https://doi.org/10.1016/j.strusafe.2011.07.001.

Davenport, A.G., 1983. The relationship of reliability to wind loading. J. Wind Eng. Ind. Aerod. 13 (1–3), 3–27. https://doi.org/10.1016/0167-6105(83)90125-3.

Dee, D.P., et al., 2011. The ERA-Interim reanalysis: configuration and performance of the data assimilation system. Q. J. R. Meteorol. Soc. 137 (656), 553–597. https://doi.org/10.1002/qj.828.

Fenerci, A., Øiseth, O., 2017. Measured buffeting response of a long-span suspension bridge compared with numerical predictions based on design wind spectra. J. Struct. Eng. 143 (9), 04017131 https://doi.org/10.1061/(asce)st.1943-541x.0001873.

Fenerci, A., Øiseth, O., 2018. Site-specific data-driven probabilistic wind field modeling for the wind-induced response prediction of cable-supported bridges. J. Wind Eng. Ind. Aerod. 181, 161–179. https://doi.org/10.1016/j.jweia.2018.09.002. June.

Fenerci, A., Øiseth, O., Rønnquist, A., 2017. Long-term monitoring of wind field characteristics and dynamic response of a long-span suspension bridge in complex terrain. Eng. Struct. 147, 269–284. https://doi.org/10.1016/j.engstruct.2017.05.070.

Fitzwater, L.R.M., Cornell, C.A., Veers, P.S., 2003. Using Environmental Contours to Predict Extreme Events on Wind Turbines. ASME 2003 Wind Energy Symp. Wind., pp. 244–258. https://doi.org/10.1115/wind2003-865

Furevik, B.R., Agustsson, H., Lauen Borg, A., Midjiyawa, Z., Nyhammer, F., Gausen, M., 2020. Meteorological observations in tall masts for the mapping of atmospheric flow in Norwegian fjords. Earth Syst. Sci. Data 12 (4), 3621–3640. https://doi.org/10.5194/essd-12-3621-2020.

Gumbel, E.J., 1958. Statistics of Extremes. Columbia University Press, New York.

Hannesdóttir, Á., Kelly, M., Dimitrov, N., 2019. Extreme wind fluctuations: joint statistics, extreme turbulence, and impact on wind turbine loads. Wind Energy Sci 4 (2), 325–342. https://doi.org/10.5194/wes-4-325-2019.

Harper, B., Kepert, J., Ginger, J., 2009. 4B . 1 WIND SPEED TIME AVERAGING CONVERSIONS FOR TROPICAL CYCLONE, pp. 6–8. June 2014.

Haselsteiner, A.F., Ohlendorf, J.H., Wosniok, W., Thoben, K.D., 2017. Deriving environmental contours from highest density regions. Coast. Eng. 123, 42–51. https://doi.org/10.1016/j.coastaleng.2017.03.002. March.

Hasofer, A.M., Lind, N.C., 1974. An exact and invariant first order reliability format. J. Eng. Mech. Div. 100, 111–121. July.

Haver, S., Winterstein, S.R., 2009. Environmental contour lines: a method for estimating long term extremes by a short term analysis. Trans. - Soc. Nav. Archit. Mar. Eng. 116, 116–127. January.

Heredia-Zavoni, E., Montes-Iturrizaga, R., 2019. Modeling directional environmental contours using three dimensional vine copulas. Ocean Eng. 187, 106102. https://doi.org/10.1016/j.oceaneng.2019.06.007. July 2018.

Kaimal, J.C., Wyngaard, J.C., Izumi, Y., Coté, O.R., 1972. Spectral characteristics of surface-layer turbulence. Q. J. R. Meteorol. Soc. 98 (417), 563–589. https://doi.org/10.1002/qj.49709841707.

Kareem, A., 1987. Wind effects on structures: a probabilistic viewpoint. Probabilist. Eng. Mech. 2 (4), 166–200. https://doi.org/10.1016/0266-8920(87)90009-9.

Karmakar, D., Bagbanci, H., Guedes Soares, C., 2016. Long-term extreme load prediction of spar and semisubmersible floating wind turbines using the environmental contour method. J. Offshore Mech. Arctic Eng. 138 (2), 1–9. https://doi.org/10.1115/1.4032099.

Klemp, J.B., Skamarock, W.C., Dudhia, J., 2007. Conservative split-explicit time integration methods for the compressible nonhydrostatic equations. Mon. Weather Rev. 135 (8), 2897–2913. https://doi.org/10.1175/MWR3440.1.

Li, Q.S., Li, X., Chan, P.W., 2021. Impact of a fifty-year-recurrence super typhoon on skyscrapers in Hong Kong: large-scale field monitoring study. J. Struct. Eng. 147 (3), 04021004 https://doi.org/10.1061/(asce)st.1943-541x.0002930.

Lieblein, J., 1974. Efficient Lillethods of Extreme-Value Methodology.

Loth, C., Baker, J.W., 2015. Environmental contours for determination of seismic design response spectra. In: 12th Int. Conf. Appl. Stat. Probab. Civ. Eng. ICASP 2015.

Lystad, T.M., Fenerci, A., Øiseth, O., 2018. Evaluation of mast measurements and wind tunnel terrain models to describe spatially variable wind field characteristics for long-span bridge design. J. Wind Eng. Ind. Aerod. 179, 558–573. https://doi.org/10.1016/j.jweia.2018.06.021. June.

Lystad, T.M., Fenerci, A., Øiseth, O., 2020. Buffeting response of long-span bridges considering uncertain turbulence parameters using the environmental contour method. Eng. Struct. 213, 110575. https://doi.org/10.1016/j.engstruct.2020.110575. March.

Lystad, T.M., Fenerci, A., Øiseth, O., 2021. Long-term extreme buffeting response of cable-supported bridges with uncertain turbulence parameters. Eng. Struct. 236 https://doi.org/10.1016/j.engstruct.2021.112126. March.

Michalakes, et al., 2001. Development of a next generation regional weather research and forecast model. Developments in teracomputing. https://doi.org/10.1142/4819.

Midjiyawa, Z., Cheynet, E., Reuder, J., Ágústsson, H., Kvamsdal, T., 2021. Potential and challenges of wind measurements using met-masts in complex topography for bridge design: Part I – integral flow characteristics. J. Wind Eng. Ind. Aerod. 211 https://doi.org/10.1016/j.jweia.2021.104584.

Moan, T., Gao, Z., Ayala-Uraga, E., 2005. Uncertainty of wave-induced response of marine structures due to long-term variation of extratropical wave conditions. Mar. Struct. 18 (4), 359–382. https://doi.org/10.1016/j.marstruc.2005.11.001.

Montes-Iturrizaga, R., Heredia-Zavoni, E., 2015. Environmental contours using copulas. Appl. Ocean Res. 52, 125–139. https://doi.org/10.1016/j.apor.2015.05.007.

Moriarty, P.J., Holley, W.E., Butterfield, S., 2002. Effect of turbulence variation on extreme loads prediction for wind turbines. J. Sol. Energy Eng. Trans. ASME 124 (4), 387–395. https://doi.org/10.1115/1.1510137.

Naess, A., Moan, T., 2012. Stochastic Dynamics of Marine Structures. Cambridge University Press, Cambridge.

Naess, A., Gaidai, O., Karpa, O., 2013. Estimation of extreme values by the average conditional exceedance rate method. J. Probab. Stat. https://doi.org/10.1155/2013/797014.

Niedzwecki, J.M., Van De Lindt, J.W., Yao, J.T.P., 1998. Estimating extreme tendon response using environmental contours. Eng. Struct. 20 (7), 601–607. https://doi.org/10.1016/S0141-0296(97)00061-8.

Norwegian Meteorological Institute, 2020. Observasjonsdata i SVV-E39-prosjektet. https://thredds.met.no/thredds/catalog/obs/mast-svv-e39/catalog.html.

Pagnini, L., 2010. Reliability analysis of wind-excited structures. J. Wind Eng. Ind. Aerod. 98 (1), 1–9. https://doi.org/10.1016/j.jweia.2009.08.010.

Pagnini, L.C., Solari, G., 2002. Gust buffeting and turbulence uncertainties. J. Wind Eng. Ind. Aerod. 90 (4–5), 441–459. https://doi.org/10.1016/S0167-6105(01)00202-1.

Raed, K., Teixeira, A.P., Guedes Soares, C., 2020. Uncertainty assessment for the extreme hydrodynamic responses of a wind turbine semi-submersible platform using different environmental contour approaches. Ocean Eng. 195, 106719. https://doi.org/10.1016/j.oceaneng.2019.106719. April 2019.

Rosenblatt, M., 1952. Remarks on a multivariate transformation author (s): murray Rosenblatt published by : Institute of mathematical statistics stable. Ann. Math. Stat. 23 (3), 470–472. REFERENCES Linked references are available on JSTOR for this article. http://www.jstor.org/stable/2236692.

Saranyasoontorn, K., Manuel, L., 2004. From the environmental contour method. Eng. Conf. 1, 128–135.

Saranyasoontorn, K., Manuel, L., 2006. Design loads for wind turbines using the environmental contour method. J. Sol. Energy Eng. Trans. ASME 128 (4), 554–561. https://doi.org/10.1115/1.2346700.

Seo, D.W., Caracoglia, L., 2012. Statistical buffeting response of flexible bridges influenced by errors in aeroelastic loading estimation. J. Wind Eng. Ind. Aerod. 104 (106), 129–140. https://doi.org/10.1016/j.jweia.2012.03.036.

Seo, D.W., Caracoglia, L., 2013. Estimating life-cycle monetary losses due to wind hazards: fragility analysis of long-span bridges. Eng. Struct. 56, 1593–1606. https://doi.org/10.1016/j.engstruct.2013.07.031.

Skamarock, W.C., et al., 2008. A description of the advanced research WRF version 3. Powers, J. G.

Solari, G., 1997. Wind-excited response of structures with uncertain parameters. Probabilist. Eng. Mech. 12 (2), 75–87. https://doi.org/10.1016/s0266-8920(96)00027-6.

Solari, G., Piccardo, G., 2001. Probabilistic 3-D turbulence modeling for gust buffeting of structures. Probabilist. Eng. Mech. 16 (1), 73–86. https://doi.org/10.1016/S0266-8920(00)00010-2.

Ucar and, D.T.C., 2013. The weather research and forecast model. http://www.wrf-model.org/index.php.

van de Lindt, J.W., Niedzwecki, J.M., 1997. Sensitivity of TLP tendon reliability estimates to excitation by multi-peaked random seas. Proc. Int. Offshore Polar Eng. Conf. 4, 139–144.

Van De Lindt, J.W., Niedzwecki, J.M., 2000. Environmental contour analysis in earthquake engineering. Eng. Struct. 22 (12), 1661–1676. https://doi.org/10.1016/S0141-0296(99)00114-5.

Vanem, E., 2019. 3-Dimensional environmental contours based on a direct sampling method for structural reliability analysis of ships and offshore structures. Ships Offshore Struct. 14 (1), 74–85. https://doi.org/10.1080/17445302.2018.1478377.

Vegvesen, Statens, 2016. E39 Sulafjorden Multispan Suspension Bridge Om GBS Feasibility Studies-Presentation [Online]. Available: https://www.vegvesen.no/_attachment/1545452/binary/1135150?fast_title=16+Flerspenns+hengebru+på+fast+fundament+%28GBS%29.pdf.

Velarde, J., Vanem, E., Kramhøft, C., Sørensen, J.D., 2019. Probabilistic analysis of offshore wind turbines under extreme resonant response: application of environmental contour method. Appl. Ocean Res. 93, 101947. https://doi.org/10.1016/j.apor.2019.101947. September.

Vindteknikk, Kjeller, og Vartdalsfjorden, Sulafjorden, 2018. Møre Og Romsdal Analyse Av Modellert Vind. strøm og bølger for.

Wang, H., Li, A., Niu, J., Zong, Z., Li, J., 2013. Long-term monitoring of wind characteristics at Sutong Bridge site. J. Wind Eng. Ind. Aerod. 115, 39–47. https://doi.org/10.1016/j.jweia.2013.01.006.

Winterstein, S.R., Ude, T.C., a Cornell, C., Bjerager, P., Haver, S., 1993. Environmental parameters for extreme response: inverse form with omission factors. Icossar- 93, 9–13. August.